Journal of Alloys and Compounds 770 (2019) 981–988

Contents lists available at ScienceDirect

Journal of Alloys and Compounds

journal homepage: http://www.elsevier.com/locate/jalcom

From magnetic cubic pre-kesterite to semiconducting tetragonal kesterite Cu_2ZnSnS_4 nanopowders *via* the mechanochemically assisted route

Katarzyna Kapusta [a], Mariusz Drygas [a], Jerzy F. Janik [a, *], Piotr Jelen [b], Miroslaw M. Bucko [b], Zbigniew Olejniczak [c]

[a] AGH University of Science and Technology, Faculty of Energy and Fuels, Al. Mickiewicza 30, 30-059, Krakow, Poland
[b] AGH University of Science and Technology, Faculty of Materials Science and Ceramics, Al. Mickiewicza 30, 30-059, Krakow, Poland
[c] Institute of Nuclear Physics, Polish Academy of Sciences, Ul. Radzikowskiego 152, 31-342, Krakow, Poland

ARTICLE INFO

Article history:
Received 8 June 2018
Received in revised form
31 July 2018
Accepted 16 August 2018
Available online 17 August 2018

Keywords:
Kesterite
Mechanochemical synthesis
Nanopowders
Photovoltaics

ABSTRACT

Presented is a study on the mechanochemically assisted synthesis of kesterite Cu_2ZnSnS_4 from the elements for photovoltaic applications. Initial application of high energy ball milling under selected conditions, including the highest achievable rotation speeds up to 1000 rpm, affords a pure cubic nanophase with the nominal kesterite composition. The phase is tentatively called a pre-kesterite and it is shown by EPR to be magnetic. Accordingly, it does not produce either ^{65}Cu or ^{119}Sn MAS NMR spectra. Also, the material shows no well-defined absorption in the UV–vis range and, based on this, does not exhibit definite semiconducting properties. The highly disordered and defected structure with random metal site occupation originated in the mechanochemical synthesis step is proposed to account for the observed properties of pre-kesterite. Upon subsequent pyrolysis under argon at temperatures above 300 °C, preferably at around 500 °C, the cubic phase is converted to the tetragonal phase of kesterite, apparently, by metal site reconfiguration. The annealed nanopowders show the expected ^{65}Cu and ^{119}Sn MAS NMR characteristics. The Raman spectra support similar bonding environment and lattice phonon characteristics for both related phases as well as the eventual formation of kesterite nanopowders whereas their UV–vis spectra provide the direct band gap in the range of 1.35–1.48 eV, typical for semiconducting kesterite.

1. Introduction

The quaternary metal sulfide Cu_2ZnSnS_4, referred to as kesterite or CZTS, and the related stannite Cu_2FeSnS_4 have been in recent years a subject of an intensive upfront research encompassing both synthesis/characterization and utilization trials in inexpensive, highly efficient, and environmental-friendly photovoltaic devices [1–4]. It appears that in kesterite sulfur S can be partially or totally replaced by selenium Se and zinc Zn by iron Fe leading to increased cell efficiencies. For device applications, thin film formation including vacuum-based techniques (sputtering, evaporation) or nanoparticle ink applications (electrodeposition, powder metallurgy) is usually applied. In the latter, kesterite nanopowders may be used as the inorganic part of nano-contacts of the inorganic-organic photovoltaic cell. For elucidation of fundamental properties, single crystals or micro- and nanocrystalline powders are preferably synthesized. In this regard, there are still some challenging research targets to be revisited and explored to name such issues as development of a simple, reproducible, and cost-effective synthesis method(s) including the preparation of nanopowders, clarification of the interplay between the structure/lattice disorder/composition features and optical properties as well as, on the application side, a need for increased kesterite-based cell efficiencies.

There are published somewhat confusing reports on kesterite composition and crystal structure/lattice order-disorder issues. The problem has been addressed both theoretically [5–7] and experimentally [8–12]. It appears that kesterite can tolerate a certain degree of lattice defects and metal position disorder, which impacts cell point group symmetry and, consequently, the macroscopic

* Corresponding author.
E-mail address: janikj@agh.edu.pl (J.F. Janik).

https://doi.org/10.1016/j.jallcom.2018.08.135
0925-8388/

crystal structure. Due to similar mass/size characteristics of the metal centers Cu(I) and Zn (II), the powder XRD determinations can provide with only limited information on detailed structural features. Regardless of this, there are available quite a few XRD studies reporting kesterite materials as orthorhombic [13], hexagonal (wurzite) [14,15], or tetragonal of kesterite- or stannite-type [16–18], the latter including the synchrotron radiation X-ray diffraction report [19]. In the case of the kesterite phase of many as-prepared materials, it is not uncommon, especially, for small particles with sizes below some 10 nm to treat it as tetragonal despite the apparent cubic (sphalerite-type) appearance of the XRD patterns [20–23]. In this regard, not easily available neutron scattering measurements can in principle shed more light into the structural details and order-disorder of site occupation of the evolving kesterite in multistep reaction pathways with an essential thermal annealing step [8,24]. Similarly, the TEM/SAED/CBED case-study examination of both the as-prepared and thermally annealed kesterite samples pointed out to complex structure characteristics of the basically tetragonal phase that may include extensive lamellar twinning and associated local hexagonal domains [17]. EXAFS measurements for the kesterite Cu_2ZnSnS_4 – stannite Cu_2FeSnS_4 solid solutions enabled determination of the prevailing oxidation state of iron as Fe (II) [25] whereas for pure powders of kesterite the oxidation state of tin was confirmed to be Sn (IV) [26]. In general, rare synchrotron spectroscopies (XANES, EXAFS) seem indispensable when coordination symmetry and chemical state of atoms are of concern as definitely is the case of the compositionally/structurally complex kesterite. Additionally, there is a great potential in applications of Raman spectroscopy, especially, from a viewpoint of potential binary and ternary metal sulfide contaminants in the kesterite materials [15,21,27–30]. Also, solid state NMR measurements that sample nuclei close range/local chemical environment have come to play recently a significant role in elucidation of the kesterite composition and purity [30–32].

High energy ball milling can often induce chemical reactions in the mechanically treated system which are then called, accordingly, mechanochemical reactions [20,33,34]. The method is simple, automated, and convenient to perform but may have, potentially, one downside of unintentionally introducing small quantities of contaminants due to milling ball abrasion. The latter can be minimized by using a liquid process medium (wet milling). Other important processing factors include the number and size of milling balls, substrate weight, rotation speed, and milling time. This method has been tried a few times for kesterite powder synthesis both for achieving practical goals by making prototype photovoltaic cells and for more fundamental studies of the relevant reaction systems and product properties. Such a classification, at first glance, may be somewhat artificial but it reflects the history of the ball milling-assisted synthesis of kesterite. The optimum conditions for efficient ball milling are presently offered by planetary ball mills with the limiting speeds of up to 1000–1100 rpm.

The mechanochemically milled at 450 rpm constituent elements (applying either S or Se) were used to make thin films of the raw product on glass supports to be subsequently annealed at 300–700 °C [35]. Depending on milling time of up to 30 h, the milled powders were either mixtures of sulfides/selenides or the supposed cubic CZTS/CZTSe whereas the second step high temperature treatment was reported to cause mainly grain growth. Similarly, milling the elements of a selected non stoichiometric ratio at 290 and 580 rpm for up to 48 h resulted under favorable conditions in the apparent cubic phase called the CZTS phase [36]. Sintering/annealing of pressed pellets of such raw powders at 500–700 °C caused grain growth with no clear-cut tetragonal polytype evolution from the cubic precursor. A mechanochemical route to single phase CZTS powder was also described in two other reports [20,37]. In these cases, the component binary metal sulfides were dry-milled at 400 rpm for 3 h and the resulting poorly crystalline cubic product was further annealed at 500 °C to yield a tetragonal phase of kesterite. Other reports were concerned with the mechanochemically assisted synthesis method for the related stannite Cu_2FeSnS_4 [38] and $Cu_2ZnSnTe_4$ [39] and confirmed the general utility of the method.

Herein, a comprehensive approach to the mechanochemically assisted synthesis of kesterite from the elements at the highest practically achievable rotation speeds is reported. A fundamental difference in properties of the raw cubic powders from the mechanochemical milling step and the final tetragonal kesterite products from the crucial thermal annealing at increased temperatures lays the grounds for the concept of the former as pre-kesterite with completely metal site disordered/averaged out positions to exhibit no definite semiconducting but magnetic properties.

2. Experimental

2.1. Synthesis

(1) **First step - mechanochemical milling.** Weighted amounts of commercially available powders of copper Cu, zinc Zn, tin Sn, and sulfur S (Avantor Performance Materials Poland S.A.) of the close to 2:1:1:4 stoichiometric ratio (typically, 2 at.% excess of S) and totalling *ca.* 7 g were placed in the 20 mL grinding bowl of planetary micro mill Pulverisette 7 (Fritsch) together with a set of 80 tungsten carbide WC of 5 mm in diameter balls and 6–7 mL of xylene as a dispersion fluid. The effective milling time ranged from 1 to 20 h, which was realized by 3-minute milling cycles each followed by a 10-minute idle period to prevent from bowl overheating. The rotation speed was 900 or 1000 rpm; the latter was the highest achievable speed with the applied set of the bowl and balls. After milling, the bulk of solvent was evaporated/dried at room temperature and the resulting black solid was transferred to a flask to be further evacuated for 1 h.

(2) **Second step - pyrolysis.** After sampling the raw product for characterization, it was subjected to pyrolysis in an alumina boat crucible for 6 h under an argon flow of 0.05 L/min at temperatures ranging from 200 to 800 °C. The off-black product was evacuated for 0.5 h at room temperature to afford the target material.

2.2. Characterization

All products were characterized by standard powder XRD analysis (Empyrean PANalytical, Cu K_α source; $2\Theta = 10–110°$). Average crystallite sizes were evaluated from Scherrer's equation applying the Rietveld refinement method. Helium densities were obtained by Micromeritics AccuPyc. Selected materials were investigated by photoelectron spectroscopy XPS (Vacuum Systems Workshop Ltd., Mg anode with photon energy of 1253.6 eV). Solid state MAS NMR spectra were measured on the APOLLO console (Tecmag) at the magnetic field of 7.05 T produced by the 300 MHz/89 mm superconducting magnet (Magnex). A Bruker HP-WB high-speed MAS probe equipped with the 4 mm zirconia rotor and KEL-F cap was used to spin the sample. The ^{65}Cu MAS NMR spectra were measured at 85.11 MHz using a single 2 μs rf pulse corresponding to $\pi/4$ flipping angle in the liquid. The spinning speed was 6 kHz. The acquisition delay used in accumulation was equal to 10 s and 256 scans were acquired. The frequency scale in ppm was referenced to the ^{65}Cu resonance of CuCl. The ^{119}Sn MAS NMR spectra were measured at 111.68 MHz using a single 3 μs rf pulse corresponding

to π/2 flipping angle. The spinning speed was 6 kHz. The acquisition delay used in accumulation was 30 s and 256 scans were acquired. The frequency scale in ppm was referenced to the central transition of SnS spectrum located at −299 ppm. Micro-Raman analysis was done by HORIBA LabRAM HR spectrometer with 532 nm laser, sample power of 20 mW, accumulation time 10 s and 2 scans, confocal hole 1000 μm with long-focus length. UV–vis data were collected in the diffuse reflectance mode on a Perkin-Elmer spectrophotometer Lambda 35 equipped with a 50 mm integrating sphere. A disk made of pure $BaSO_4$ was used for background collection whereas a thin layer of product powder pressed on the disc surface was used for sample acquisition. SEM/EDX data were acquired with a Hitachi Model S-4700 scanning electron microscope.

3. Results and discussion

It is instructive to note that the reaction system used in kesterite formation is rather complex by including a mixture of four starting elements at once. The three applied metals, Zn, Cu, and Sn have advantageous while different affinities for the reaction with sulfur S as approximated by the respective standard enthalpies of sulfide formation Δ_fH^o (kJ/mol) [40]: ZnS, −157; Cu_2S, −46; CuS, −53; SnS, −98; SnS_2, -121. There is also a pronounced thermodynamic driving force for the formation of kesterite Cu_2ZnSnS_4 from the elements supported by its Δ_fH^o value of *ca.* −370 kJ/mol. However, one has to keep in mind that the metal particle surfaces are oxygen passivated, especially, if tin is concerned, which will impose an additional activation barrier for sulfurization reactions. Accordingly, the chemistry of the four starting elements is anticipated to be very complex and may involve numerous binary and ternary intermediates. [41]. In this regard, suitably high activation energies and/or long reaction times may be the hallmarks of kesterite synthesis in the solid state.

The wet high energy ball milling of the constituent element mixtures was performed using for the first time the highest achievable speeds in laboratory practice, *i.e.*, 900 or 1000 rpm which resulted in significant shortening of reaction time and, in favorable cases, complete reactions in the system producing a single product. While milling times from 1 to 20 h were tried, 4–10-h millings were found sufficient to yield mostly the cubic phase of the raw product at this stage. Typically, a 2 at.% excess of S was used to assure its accessibility but 10 and 50 at.% were also tried assuming that any unreacted S would be removed as volatiles during the subsequent annealing step. In the pool of a few dozens of milling experiments, only in one case a single WC ball has incidentally shattered to contaminate the raw product; otherwise, plausible ball abrasion was minimized and, in fact, undetectable due to the application of the xylene dispersion fluid.

The annealing under argon at various temperatures spanning in some cases 200–800 °C was applied to test stability and/or thermally induced changes of raw products formed in the milling step. No unequivocal reactions were detected up to *ca.* 400 °C whereas clear signs of kesterite decomposition were seen above 700 °C. The optimum conditions for the formation of the target tetragonal kesterite were narrowed to temperatures in the 450–550 °C range and 1–6 h hold times.

The effect of milling time ranging from 1 to 20 h at 900 rpm is illustrated in the XRD patterns shown in the top section of Fig. 1. The results for the raw milled powders are displayed on the left and for the annealed powders on the right. For the former, they are satisfactorily indexed to include the dominant cubic phase (sphalerite-type), 92–100%, with the *a* constant in the range of 5.42–5.45 Å and average crystallite sizes *D* of 8–12 nm. The only unreacted component is found to be elemental tin Sn, *ca.* 8% for the 1 h milling, of which some 1% persists through 4 h and, then, is below the detection limit after 10 h (not shown) and 20 h. The XRD patterns for the annealed products, 500 °C, 6 h, consistently include the tetragonal phase of kesterite with an average crystallite size 30–60 nm and some contamination by tin dioxide SnO_2. The more unreacted tin was in the raw powders, the higher was the percentage of the oxide in the annealed product. Since the annealing was carried out under strict anaerobic conditions, the presence of SnO_2 is thought to originate from adventitious oxidation of nano-tin during post-synthesis sample exposure to air. On one occasion, a sample for XRD was prepared in the dry-box under argon in the form of a thick paste in mineral oil to hinder oxidation and the resulting pattern has shown relatively much less of the oxide than in an unprotected sample. The results imply that suitably long milling times in the range 10–20 h are necessary for complete reactions with the tin component being the most sluggish to enter the quaternary lattice. They also plainly prove that under the applied milling conditions the formation of the tetragonal kesterite requires an additional thermal treatment at increased temperatures in the range 450–550 °C.

Fig. 1 includes also the relevant XRD patterns for the materials prepared at the higher milling speed of 1000 rpm, the highest one that could be achieved with the applied milling balls. The raw milled powder is now a pure cubic phase, a = 5.42 Å, D = 9 nm with no detected tin to be advantageously compared with the 900 rpm cases. Remarkably, the annealed product is a pure tetragonal kesterite with a = 5.43 Å, c = 10.84 Å, and D = 28 nm, which this time is not contaminated by tin oxide.

It is worth to mention that such a sphalerite-type cubic phase observed here for the raw powders has been quite often "misinterpreted" to belong to tetragonal kesterite – the highest intensity diffractions match in both patterns and a few specific low intensity peaks for the tetragonal phase at 2Θ below 25° have been assumed, apparently, too broad to be detected for the nanocrystalline products [20–23]. In our opinion, such an approach is too far stretched even considering the remarkable relation of the lattice parameters for the "pseudocubic" tetragonal kesterite with random Cu/Zn position distribution in the Cu-Zn metal center layers (I42m, Ref. code 96-900-4751), a = 5.4340 Å, c = 10.856 Å, where *c* is very close to *2a* [17,42]. In this regard, the *a* constant for sphalerite ZnS is 5.4110 Å and significantly differs from the respective values determined in this study, 5.42–5.45 Å. The higher *a* constants imply both bigger atoms than zinc such as tin and/or highly defected structures in the sphalerite-type lattice. Our attempts of various phase assignments consistently resulted in the cubic phase being the best solution. Based on these results supported by further characterization data (see, below) we tentatively propose that the raw product from the mechanochemical milling step is a pre-kesterite – a cubic phase made of randomly distributed atoms of Cu, Zn, and Sn in all of the metal layers of the model kesterite. Such a phase appears to tolerate, especially, a certain degree of Sn deficiency with respect to the Cu_2ZnSnS_4 stoichiometry without losing its coherence or cubic symmetry features. The incorporation of more and more Sn requires suitably long milling times and, eventually, leads to the stoichiometric cubic pre-kesterite. This chemistry pathway appears to be independent on an availability of sulfur in the starting mixture – in the systems with 10 and 50 at.% excess S and 4 h milling time, a few percent of unreacted tin is consistently detected. In conclusion, it appears that the applied high energy ball milling conditions and up to 20 h milling times are sufficient for the elements to react towards the 8–12 nm cubic crystallites of the pre-kesterite whereas deficient in supplying enough energy at this stage to support metal center reconfiguration into the distinct Cu-Zn and Cu-Sn metal layers forming the target tetragonal kesterite structure [17–19]. The

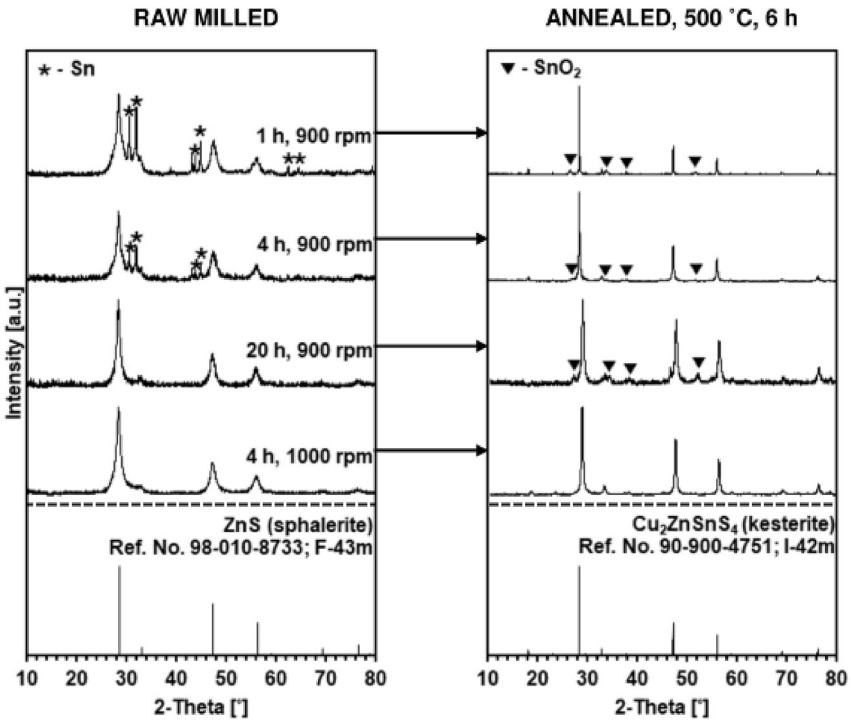

Fig. 1. XRD patterns of {2Cu+Zn+Sn+4S} powder mixtures milled at 900 or 1000 rpm, 2 at.% excess of S, milling times: 1 h, 4 h, 20 h and subsequently annealed at 500 °C, 6 h. Bar charts for cubic ZnS (sphalerite) and tetragonal kesterite are shown in the bottom.

specific assignment of the kesterite structure as belonging to the space group I-42m is typical for the so-called disordered kesterite where Cu and Zn at specific planes are randomly distributed [18].

The characteristic SEM images of the powders are included in Fig. 2. The raw powder after milling shows a relatively uniform distribution of the smallest particles of which some appear to be

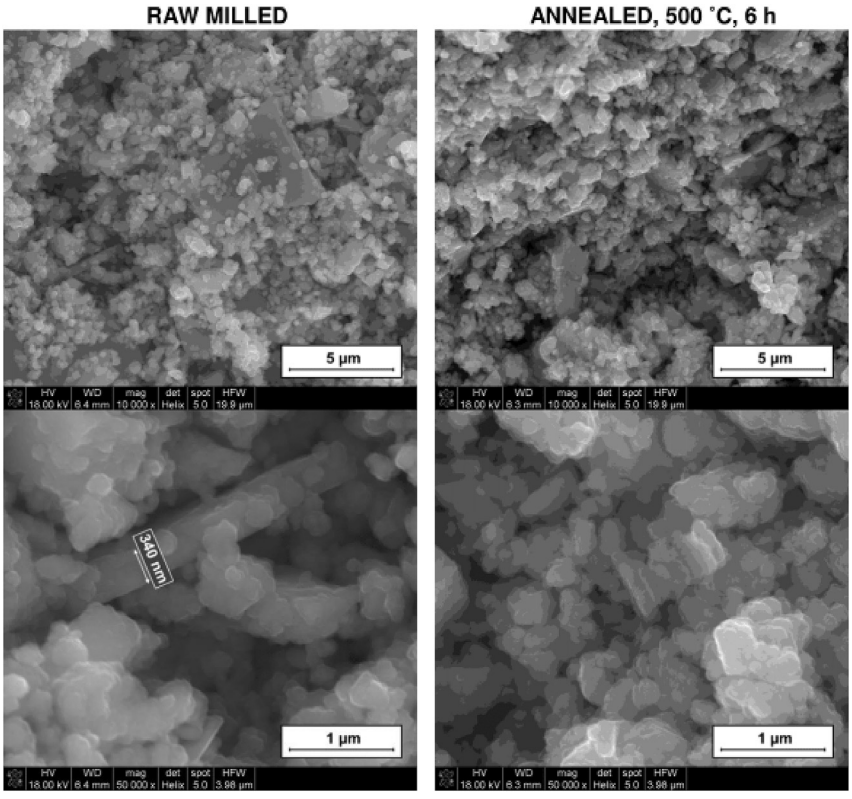

Fig. 2. SEM images of the powders of raw milled pre-kesterite −1000 rpm, 4 h, 2 at.% excess S (left) and the resulting annealed kesterite − 500 °C, 6 h (right).

tightly agglomerated as if fused into larger shapes. There are also fragments of what seems to be dense shells several hundred nanometer thick that also are agglomerates of much smaller crystallites. The shells could likely originate from material layers pressed with high energy by rotating balls against the grinding bowl surface. Very much similar morphology although with fewer shell-like fragments is exhibited in the annealed powder of kesterite supporting tight crystallite agglomeration within the larger particles. Cu, Zn, Sn, S element mapping (not shown) consistently displays very uniform distribution of all the elements, which confirms chemical homogeneity on this scale.

The helium densities for the powders of the pre-kesterite and kesterite shown in Fig. 2 are in both cases equal to 3.94 g/cm^3. For a larger pool of samples, the density ranges of 3.94–3.99 g/cm^3 for pre-kesterite and of 3.94–4.03 g/cm^3 for kesterite were recorded. These values are consistent with very similar density characteristics for both types of materials. It is instructive to compare them with the calculated 4.56 g/cm^3 for the bulk synthetic kesterite with tetragonal (stannite) structure and 4.09 g/cm^3 for bulk sphalerite ZnS [43]. In this regard, the discrepancy between the bulk and the measured helium densities can be ascribed to presence of closed/helium inaccessible pores in the agglomerates, which is quite typical for nanopowders and in some cases may be correlated with a XRD-derived crystallite size [44]. However, such an effect is clearly seen for very small particle sizes usually less than 5–10 nm, as encountered in the pre-kesterite, whereas for larger sizes the agglomeration seems to be not as tight and the helium densities reflect more the true densities. This implies that yet another factor likely associated with distinct structural defects may contribute to the density of the annealed kesterite with average crystallite sizes of several tens of nanometers.

The typical micro-Raman spectra for the products are presented in Fig. 3. The striking feature is a close resemblance, on the one hand, of the spectra for all cubic pre-kesterite materials independent on the time and speed of milling or sulfur excess (left stack) and, on the other hand, of the spectra for the resulting from them kesterite products (right stack). This appears to be true not only for the two subsets separately but also extends in between them. In this regard, the peaks for the pre-kesterite are relatively broader and more superimposed. The peaks for kesterite are generally narrower and the weak peak at the lower wavenumbers next to the strongest peak is clearly separated from it. The spectra of pre-kesterite can be satisfactorily deconvoluted into three peaks at 295-305 cm^{-1} (broad, weak), 328-332 cm^{-1} (sharp, strong), and 348-353 cm^{-1} (broad, weak). And respectively, the spectra for kesterite yield three peaks at 285-290 cm^{-1} (sharp, weak), 328–333 (sharp, strong), and 350-360 cm^{-1} (broad, weak). In the case of kesterite, yet a better fit is obtained with one more broad peak in the range 295–305 cm^{-1}, which overlaps with the already listed sharper peak there.

Since XRD measurements are of somewhat limited value when it comes to determine the impact on the kesterite structure of scrambling of the size-wise similar atoms Cu and Zn, the Raman spectroscopy has often been hoped to help discriminating among plausible structures and ways the metal centers could be distributed. In this regard, the recent theoretical calculations for a few relevant tetragonal polymorphs show many closely spaced Raman peaks that may be difficult to unequivocally pinpoint, given possible peak broadening and shifting for the nanosized and defected crystallites [45]. The calculated three most intense peaks are of A symmetry and expected at 285–289, 304–306, and 334-338 cm^{-1}. They correspond closely to the features observed in this study for the annealed kesterite of tetragonal symmetry resolved in the space group I-42m (see, above). These materials show also a very weak and broad peak in the range 350–360 cm^{-1}, which is consistent with the theoretical B-symmetry peak there. Part of discrepancies among the peak positions when comparing our results with theory could be related to the fact that the group I-42m

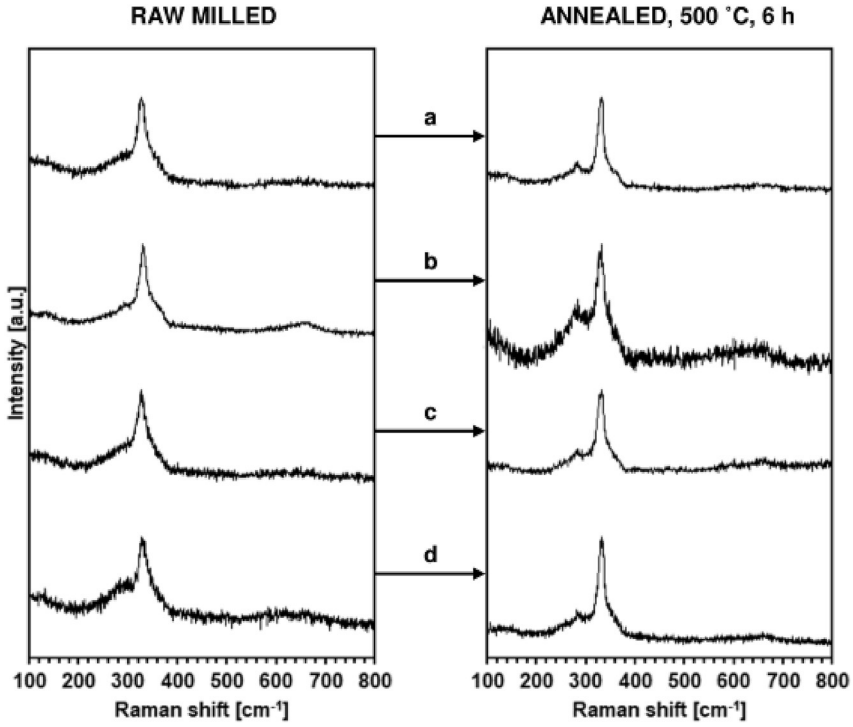

Fig. 3. Micro-Raman spectra of {2Cu+Zn+Sn+4S} products: left – after milling and right – annealed at 500 °C, 6 h: a) 900 rpm, 1 h milling, 2 at.% excess S; b) 900 rpm, 4 h milling, 50 at.% excess S; c) 900 rpm, 10 h milling, 2 at.% excess S; d) 1000 rpm, 4 h milling, 2 at.% excess S.

was not included in those theoretical calculations. As far as the cubic pre-kesterite is concerned, our deconvoluted Raman spectra consist of three broad and superimposed peaks and resemble very much the spectra for the nanosized "kesterite" assigned as tetragonal while seemingly displaying by XRD the typical sphalerite-like cubic features [21,35]. It is tempting to suppose that the apparent similarity of all the Raman spectra for the materials prepared in this study including the cubic pre-kesterite and tetragonal kesterite, reflects both the closeness of their chemical make-up and similar type of lattice phonon characteristics for them.

Close range chemical environments can often be probed by NMR measurements and they were also studied by applying the solid state ^{65}Cu and ^{119}Sn MAS NMR spectroscopy. Surprisingly, no spectra could be recorded for a range of raw pre-kesterite samples whereas the task was successfully accomplished for the annealed kesterite powders. This turned our attention to possible magnetic interference that would prevent from efficient nuclear resonance to occur in the pre-kesterite. In this regard, the electron paramagnetic resonance EPR study shows strong magnetic properties of the pre-kesterite while only remnant though detectable magnetism of the related kesterite as supported by the relative position and different slopes of the relevant curves (Fig. 4). Also, the flat and rather smoothly descending with magnetic field curves are consistent with the heterogeneous and interacting/coupled paramagnetic centers, especially, in the pre-kesterite case. This phenomenon could likely reflect the definite non-stoichiometry and different degree of disorder in the structures of both materials. One of the plausible candidates for inducing such magnetism could be Cu^{+2} ions with *d9* electron configuration. However, a XPS study confirmed solely diamagnetic *d10* Cu^{+1} ions and ruled out any presence of magnetic Cu^{+2} ions in both materials. This pointed out to yet another source of magnetism encountered mainly in nanosized structures. Namely, there have been more and more recorded instances of room temperature ferromagnetism in materials such as metal oxides, nitrides, and chalcogenides that lack magnetic ions, in which the origin of magnetism is traced to structural defects/vacancies including native surface defects and structural inhomogeneity – all quite typical in nanoscale [46]. Such phenomenon is called *d0* magnetism [47] and may be responsible for the observed magnetic properties of the intrinsically disordered raw pre-kesterite powders. On the other hand, pre-kesterite's thermal annealing appears to yield larger crystallites of much more ordered and structurally homogeneous kesterite showing merely remnant magnetism of this kind as seen in Fig. 4. Interestingly, there could be also another way of explaining the lack of NMR signals for the pre-kesterite linked to large quadrupolar coupling constants of copper Cu^{+1} ions. In this regard, the diamagnetic Cu_2S (Cu^{+1} ions) has been reported to produce no detectable ^{63}Cu NMR signal at all [48]. This was proposed to result from low symmetry environment of the ions with extremely large quadrupolar coupling constants, which resulted in the second order quadrupolar interactions that broadened the signal beyond detection.

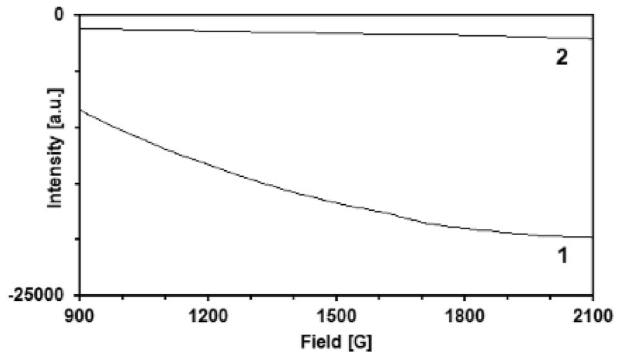

Fig. 4. EPR magnetization data for the related powders of pre-kesterite: curve 1–900 rpm, 10 h milling, 2 at.% excess S and the resulting kesterite: curve 2–500 °C, 6 h.

Fig. 5 illustrates the solid state MAS NMR selected results recorded for two kesterite samples. Both examined powders show the ^{65}Cu and ^{119}Sn resonance peaks at *ca.* 795 ppm and −123 ppm, respectively, with the latter asymmetrical in agreement with the reported data for kesterite [31,32]. A striking feature of the spectra are much lower normalized peak intensities for sample B compared with sample A. Other things being equal, this implies that in the former a significant part of atoms is not active in the NMR experiment, possibly, due to strong local magnetic interference of the type discussed earlier in the EPR section. Such an interference seems to be more pronounced for kesterite from the 500 °C-annealed sample B whereas weaker if not absent for sample A from annealing at the higher temperature of 550 °C. In this regard, based on the XRD results for kesterite powders heat treated in the range 450–550 °C, the higher is the processing temperature the better crystalline properties and larger crystallite sizes are observed. The progressing crystallization is, apparently, associated with higher local symmetry and decreasing disorder/extent of quadrupolar interactions or, alternatively, elimination of *d0* magnetism and, eventually, results in the enhancement of both nuclei NMR responses. The temperature induced emergence of a more defined local environment of the metal centers is corroborated by a relative narrowing of the NMR peaks for sample A. In this sense, NMR/EPR properties of kesterite nanopowders appear to be indispensable for digesting their structure reorganization while consistently supplementing the evolution of long range tetragonal characteristics as observed by XRD.

At this point, it is appropriate to confront the discussed analytical data for the cubic pre-kesterite – tetragonal kesterite system with determinations of the crucial property of the kesterite semiconductor, namely, its band gap from UV–vis measurements. Fig. 6 includes the acquired typical UV–vis spectra exemplified for two selected pre-kesterite – kesterite preparation routes. These are the absorption plots with inserts of the corresponding Tauc function, *i.e.*, $(\alpha h\nu)^2$ *vs.* $h\nu$ for direct transitions, where α is approximated by the Kubelka-Munk transform. The characteristic feature is the lack of a defined transition in this range for any of the cubic pre-kesterite samples and, therefore, no band-gap calculations from the Tauc plots are possible (Fig. 6, left). Therefore, within such standard UV–vis data interpretation, the raw nanopowders after milling do not appear to be unequivocally defined semiconductors. It is worth realizing that this could be, at least, partly due to very small nanoparticle sizes (*ca.* 10 nm and smaller) and the particle size distribution effect both known to impact the absorption signal in the diffuse reflectance mode. On the other hand, all tetragonal kesterite samples after annealing show similar absorption spectra from which one strong transition in the range 1.35–1.48 eV due to a direct band gap E_g can be calculated (Fig. 6, right), *i.e.*, within *ca.* 1.0–1.5 eV reported for various kesterite materials [1–4]. It is obvious that the kesterite's band gap is a variable parameter in this range and, specifically, depends on numerous experimental details that in turn decide about variations in the structural and compositional makeup of the quite flexible kesterite's tetragonal lattice.

4. Conclusions

The wet high energy ball milling of the constituent elements Cu, Zn, Sn, and S at the highest achievable rotation speeds of 900 and 1000 rpm affords paramagnetic nanopowders of compositions close to kesterite Cu_2ZnSnS_4 and of cubic crystallographic

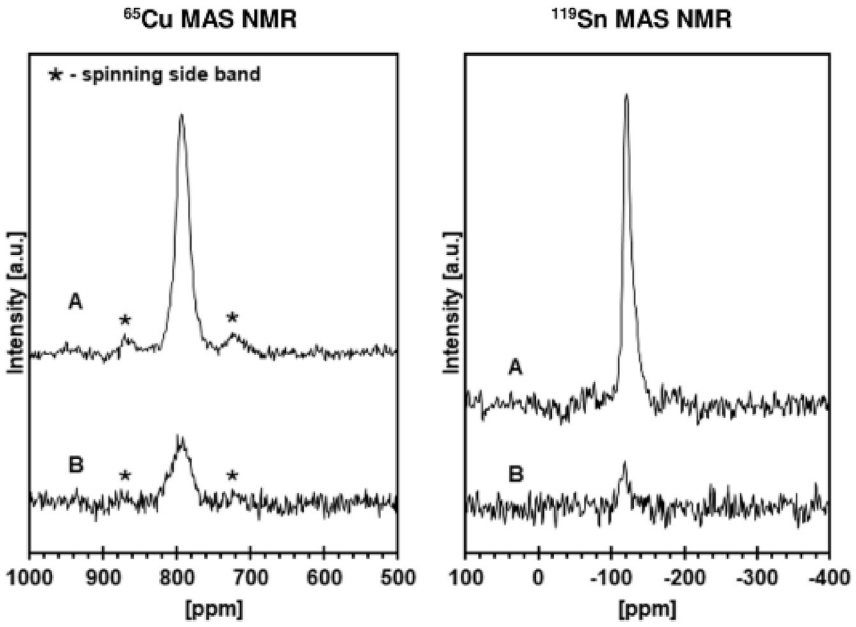

Fig. 5. Solid state ^{65}Cu (left) and ^{119}Sn (right) MAS NMR spectra for kesterite powders: A – 900 rpm, 2 at.% excess S, 4 h milling then annealed at 550 °C, 6 h; B – 900 rpm, 2 at.% excess S, 10 h milling then annealed at 500 °C, 6 h.

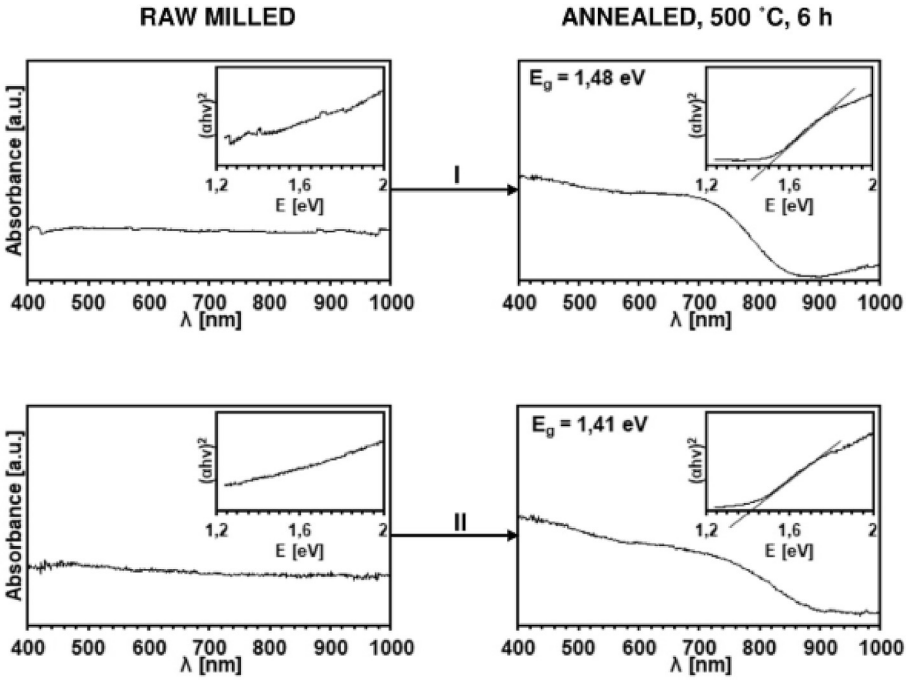

Fig. 6. UV–vis spectra with inserts of Tauc $(\alpha h\nu)^2$ *vs.* hν [energy] plots for selected pre-kesterite (left) and kesterite (right) nanopowders: I – 4 h milling, 50 at.% excess S, 900 rpm; II – 4 h milling, 2 at.% excess S, 1000 rpm.

symmetry for which no semiconductor direct band gap can be determined from UV–vis measurements. Due to overall compositional similarities, the cubic raw product formed in this mechanochemical process is tentatively called a pre-kesterite. The latter upon thermal annealing under argon, preferably, at 450–550 °C can be conveniently converted to the target kesterite nanopowder. The emergence of the definite semiconducting properties is associated with temperature-induced structural evolution from the cubic pre-kesterite to tetragonal kesterite with concomitant lapse of the materials magnetic properties. The essential kesterite properties such as a magnitude of the band gap and residual magnetism are functions of an extent/nature of non-stoichiometry accompanied by crystal lattice disorder, which are all very sensitive to variations in the mechanochemical synthesis.

Acknowledgement

Study was supported by AGH-UST Grant No. 11.11.210.373. Authors appreciate the contributions of (i) Prof. Andrzej Adamski from the Jagiellonian University, Faculty of Chemistry, Krakow, Poland, of

carrying out and interpreting EPR measurements and (ii) Prof. Kazimierz Kowalski from the AGH University of Science and Technology, Faculty of Metals Engineering and Industrial Computer Science, Krakow, Poland, of collecting and interpreting XPS data.

References

[1] Z. Shi, D. Attygalle, A.H. Jayatissa, Kesterite-based next generation high performance thin film solar cell: current progress and future prospects, J. Mater. Sci. Mater. Electron. 28 (2017) 2290–2306.

[2] X.L. Liu, Y. Feng, H.T. Cui, F.Y. Liu, X.J. Hao, G. Conibeer, D.B. Mitzi, M. Green, The current status and future prospects of kesterite solar cells: a brief review, Prog. Photovolt. Res. Appl. 24 (2016) 879–898.

[3] P. Reiss, M. Carriere, C. Lincheneau, L. Vaure, S. Tamang, Synthesis of semiconductor nanocrystals, focusing on nontoxic and earth-abundant materials, Chem. Rev. 116 (2016) 10731–10819.

[4] J. Chang, E.R. Waclawik, Colloidal semiconductor nanocrystals: controlled synthesis and surface chemistry in organic media, RSC Adv. 4 (2014) 23505–23527.

[5] P. Sarker, M.M. Al-Jassim, M.N. Huda, Theoretical limits on the stability of single-phase kesterite Cu_2ZnSnS_4, J. Appl. Phys. 117 (2015), 035702.

[6] T. Gurel, C. Sevik, T. Cagin, Characterization of vibrational and mechanical properties of quaternary compounds Cu_2ZnSnS_4 and $Cu_2ZnSnSe_4$ in kesterite and stannite structures, Phys. Rev. B 84 (2011) 205201.

[7] Y.B. Zhang, X. Yuan, X.D. Sun, B.C. Shih, P.H. Zhang, W.Q. Zhang, Comparative study of structural and electronic properties of Cu-based multinary semiconductors, Phys. Rev. B 84 (2011), 075127.

[8] A. Ritscher, M. Hoelzel, M. Lerch, The order-disorder transition in Cu_2ZnSnS_4 - a neutron scattering investigation, J. Solid State Chem. 238 (2016) 68–73.

[9] M. Valentini, C. Malerba, F. Menchini, D. Tedeschi, A. Polimeni, M. Capizzi, A. Mittiga, Effect of the order-disorder transition on the optical properties of Cu_2ZnSnS_4, Appl. Phys. Lett. 108 (2016) 211909.

[10] S.K. Samji, R. Mannam, M.S.R. Rao, Do defects get ordered in Cu_2ZnSnS_4? Scripta Mater. 117 (2016) 11–15.

[11] G. Gabka, P. Bujak, M. Gryszel, A. Ostrowski, K. Malinowska, G.Z. Zukowska, F. Agnese, A. Pron, P. Reiss, Synthesis and surface chemistry of high quality wurtzite and kesterite Cu_2ZnSnS_4 nanocrystals using tin(II) 2-ethylhexanoate as a new tin source, Chem. Commun. 65 (2015) 12985–12988.

[12] J.J.S. Scragg, L. Choubrac, A. Lafond, T. Ericson, C. Platzer-Bjorkman, A low-temperature order-disorder transition in Cu_2ZnSnS_4 thin films, Appl. Phys. Lett. 104 (2014), 041911.

[13] H.C. Jiang, P.C. Dai, Z.Y. Feng, W.L. Fan, J.H. Zhan, Phase selective synthesis of metastable orthorhombic Cu_2ZnSnS_4, J. Mater. Chem. 22 (2012) 7502–7506.

[14] J.H.N. Tchognia, Y. Arba, K. Dakhsi, B. Hartiti, J.-M. Ndjaka, A. Ridah, P. Thevenin, Solution-based deposition of wurtzite copper zinc tin sulfide nanocrystals as a novel absorber in thin film solar cells, Opt. Quant. Electron. 48 (2016) 255.

[15] Q. Zhang, M. Cao, J.S. Shen, J. Huang, Y. Zhao, Y. Sun, L.J. Wang, Y. Shen, Effect of the annealing conditions on the structural stability and photoelectrical properties of wurtzite structured Cu_2ZnSnS_4 nanoparticles, Vacuum 122 (2015) 66–74.

[16] L. Choubrac, A. Lafond, C. Guillot-Deudon, Y. Moelo, S. Jobic, Structure flexibility of the Cu_2ZnSnS_4 absorber in low-cost photovoltaic cells: from the stoichiometric to the copper-poor compounds, Inorg. Chem. 51 (2012) 3346–3348.

[17] N. Kattan, B. Hou, D.J. Fermin, D. Cherns, Crystal structure and defects visualization of Cu_2ZnSnS_4 nanoparticles employing transmission electron microscopy and electron diffraction, Appl. Mater. Today 1 (2015) 52–59.

[18] P. Bais, M.T. Caldes, M. Paris, C. Guillot-Deudon, P. Fertey, B. Domenges, A. Lafond, Cationic and anionic disorder in CZTSSe kesterite compounds: a chemical crystallography study, Inorg. Chem. 56 (2017) 11779–11786.

[19] T. Washio, H. Nozaki, T. Fukano, T. Motohiro, K. Jimbo, H. Katagiri, Analysis of lattice site occupancy in kesterite structure of Cu_2ZnSnS_4 films using synchrotron radiation x-ray diffraction, J. Appl. Phys. 110 (2011), 074511.

[20] A. Ritscher, J. Just, O. Dolotko, S. Schor, M. Lerch, A mechanochemical route to single phase Cu_2ZnSnS_4 powder, J. Alloys Compd. 670 (2016) 289–296.

[21] W. Wang, H.L. Shen, H.Y. Yao, J.Z. Li, J. Jiao, Influence of solution temperature on the properties of Cu_2ZnSnS_4 nanoparticles by ultrasound-assisted microwave irradiation, J. Mater. Sci. Mater. Electron. 26 (2015) 1449–1454.

[22] G. Rajesh, N. Muthukumarasamy, E.P. Subraman, M.R. Venkatraman, S. Agilan, V. Ragavendran, M. Thambidurai, S. Velumani, J.S. Yi, D. Velauthapillai, Solution-based synthesis of high yield CZTS (Cu_2ZnSnS_4) spherical quantum dots, Superlattice. Microst. 77 (2015) 305–312.

[23] D. Pareek, K.R. Balasubramaniam, P. Sharma, Synthesis and characterization of bulk Cu_2ZnSnX_4 (X: S, Se) via thermodynamically supported mechanochemical process, Mater. Char. 103 (2015) 42–49.

[24] A. Ritscher, A. Franz, S. Schorr, M. Lerch, Off-stoichiometric CZTS: neutron scattering investigations on mechanochemically synthesized powders, J. Alloys Compd. 689 (2016) 271–277.

[25] W. Zalewski, R. Bacewicz, J. Antonowicz, A. Pietnoczka, T.L. Evstigneeva, S. Schorr, XAFS study of kesterite, kuramite and stannite type alloys, J. Alloys Compd. 492 (2010) 35–38.

[26] R. Bacewicz, J. Antonowicz, S. Podsiadło, S. Schorr, Local structure in Cu_2ZnSnS_4 studied by the XAFS method, Solid State Commun. 177 (2014) 54–56.

[27] P. Prabeesh, I. Packia Selvam, S.N. Potty, Effect of annealing temperature on a single step processed Cu_2ZnSnS_4 thin film via solution method, Thin Solid Films 606 (2016) 94–98.

[28] M. Guc, S. Levcenko, I.V. Bodnar, V. Izquierdo-Roca, X. Fontane, L.V. Volkova, E. Arushanov, A. Perez-Rodriguez, Polarized Raman scattering study of kesterite type Cu_2ZnSnS_4 single crystals, Sci. Rep. UK 6 (2016) 19414.

[29] B.K. Durant, B.A. Parkinson, Photovoltaic response of natural kesterite crystals, Sol. Energy Mater. Sol. C 144 (2016) 586–591.

[30] M. Paris, L. Choubrac, A. Lafond, C. Guillot-Deudon, S. Jobic, Solid-state NMR and Raman spectroscopy to address the local structure of defects and the tricky issue of the Cu/Zn disorder in Cu-poor, Zn-rich CZTS materials, Inorg. Chem. 53 (2014) 8646–8653.

[31] M. Paris, G. Larramona, P. Bais, S. Bourdais, A. Lafond, C. Chone, C. Guillot-Deudon, B. Delatouche, C. Moisan, G. Dennler, ^{119}Sn MAS NMR to assess the cationic disorder and the anionic distribution in sulfoselenide $Cu_2ZnSn(S_xSe_{1-x})_4$ compounds prepared from colloidal and ceramic routes, J. Phys. Chem. C 119 (2015) 26849–26857.

[32] L. Choubrac, M. Paris, A. Lafond, C. Guillot-Deudon, X. Rocquefelte, S. Jobic, Multinuclear (^{67}Zn, ^{119}Sn and ^{65}Cu) NMR spectroscopy - an ideal technique to probe the cationic ordering in Cu_2ZnSnS_4 photovoltaic materials, Phys. Chem. Chem. Phys. 15 (2013) 10722–10725.

[33] C.P. Xu, S. De, A.M. Balu, M. Ojeda, R. Luque, Mechanochemical synthesis of advanced nanomaterials for catalytic applications, Chem. Commun. 51 (2015) 6698–6713.

[34] P. Balaz, M. Achimovicova, M. Balaz, P. Billik, Z. Cherkezova-Zheleva, J.M. Criado, F. Delogu, E. Dutkova, E. Gaffet, F.J. Gotor, R. Kumar, I. Mitov, T. Rojac, M. Senna, A. Streletskii, K. Wieczorek-Ciurowa, Hallmarks of mechanochemistry: from nanoparticles to technology, Chem. Soc. Rev. 42 (2013) 7571–7637.

[35] D. Pareek, K.R. Balasubramaniam, P. Sharma, Reaction pathway for synthesis of $Cu_2ZnSn(S/Se)_4$ via mechano-chemical route and annealing studies, J. Mater. Sci. Mater. Electron. 28 (2017) 1199–1210.

[36] C.Q. Liu, B. We, N. Wang, S.M. Liu, H.L. Wang, W.W. Jiang, W.Y. Ding, S.C. Xu, W.P. Chai, Phase evolution and sintering behaviors of Cu_2ZnSnS_4 powders synthesized by mechanochemical process with different milling parameters, J. Alloys Compd. 708 (2017) 428–436.

[37] A. Ritscher, M. Schlosser, A. Pfitzner, M. Lerch, Study of the mechanochemical process to crystalline Cu_2ZnSnS_4 powder, Mater. Res. Bull. 84 (2016) 162–167.

[38] P. Balaz, M. Balaz, M.J. Sayagues, I. Skorvanek, A. Zorkovska, E. Dutkova, J. Briancin, J. Kovac, J. Kovac Jr., Y. Shpotyuk, Mechanochemical solvent-free synthesis of quaternary semiconductor Cu-Fe-Sn-S nanocrystals, Nanoscale Res. Lett. 12 (2017) 256.

[39] D. Pareek, K.R. Balasubramaniam, P. Sharma, Synthesis and characterization of kesterite $Cu_2ZnSnTe_4$ via ball-milling of elemental powder precursors, RSC Adv. 6 (2016) 68754–68759.

[40] A.J. Jackson, A. Walsh, Ab initio thermodynamic model of Cu_2ZnSnS_4, J. Mater. Chem. A 2 (2014) 7829–7836.

[41] I.D. Olekseyuk, I.V. Dudchak, L.V. Piskach, Phase equilibria in the Cu_2S-ZnS-SnS_2 system, J. Alloys Compd. 368 (2004) 135–143.

[42] P. Bonazzi, L. Bindi, G.P. Bernardini, S. Menchetti, A model for the mechanism of incorporation of Cu, Fe and Zn in the stannite-kesterite series, Cu_2FeSnS_4-Cu_2ZnSnS_4, Can. Mineral. 41 (2003) 639–647.

[43] WWW-MINCRYST, Crystallographic and Crystallochemical Database for Minerals and Their Structural Analogues, 2018. http://database.iem.ac.ru/mincryst.

[44] M. Drygaś, J.F. Janik, Modeling porosity of high surface area nanopowders of the gallium nitride GaN semiconductor, Mater. Chem. Phys. 133 (2012) 932–940.

[45] M. Dimitrievska, F. Boero, A.P. Litvinchuk, S. Delsante, G. Borzone, A. Perez-Rodriguez, V. Izquierdo-Roca, Structural polymorphism in "kesterite" Cu_2ZnSnS_4: Raman spectroscopy and first-principles calculations analysis, Inorg. Chem. 56 (2017) 3467–3474.

[46] A. Sundaresan, C.N.R. Rao, Ferromagnetism as a universal feature of inorganic nanoparticles, Nano Today 4 (2009) 96–106.

[47] I.G. Morozov, O.V. Belousova, O.A. Belyakov, I.P. Parkin, S. Sathasivam, M.V. Kuznetcov, Titanium nitride room-temperature ferromagnetic nanoparticles, J. Alloys Compd. 675 (2016) 266–276.

[48] N. Yamakawa, M. Jiang, C.P. Grey, Investigation of the conversion reaction mechanisms for binary copper(II) compounds by solid-state NMR spectroscopy and X-ray diffraction, Chem. Mater. 21 (2009) 3162–3176.